Journal of Engineering Physics and Thermophysics, Vol. 73, No. 2, 2000

NUMERICAL AND PHYSICAL MODELING OF A LOW-VELOCITY AIR FLOW IN A CHANNEL WITH A CIRCULAR VORTEX CELL

S. A. Isaev, S. V. Guvernyuk, M. A. Zubin, and Yu. S. Prigorodov

UDC 532.517.4

Based on a numerical solution, by the finite-volume method, of two-dimensional Reynolds equations that are closed using Menter's two-parameter turbulence model and on physical modeling in a wind tunnel the authors analyze flow in a channel with a cylindrical vortex cell of circular cross section.

1. As is known, the problem of controlling flow along bodies is among pressing fundamental problems of aerohydromechanics and attracts increased attention of researchers. In this connection, the cycle of works of the last two years [1-5] on an efficient method of organizing flow using so-called trapped vortices or vortex cells mounted in the contour of the body seems very interesting.

The creation of momentum within vortex cells, in particular, due to the suction of a fluid through a wall of a central body or the rotation of a cylinder, makes it possible to change substantially the regime of flow along the object considered. It should be noted that wall layers are acted upon in comparatively small-scale regions. As a result, it seems possible to ensure unseparated flow along a thick profile (in a wide range of the Reynolds number) and a plate (with suppression of the Kármán vortex street) and, as a consequence, to reduce the drag of bodies, in particular, of a circular cylinder, and to attain a high (of the order of several tens) lift-drag ratio for the profile.

To solve the indicated problems, an efficient multiblock computational methodology is developed that is based on employing a factorized algorithm in combination with multistage and multiblock intersecting grids. This strategy is partially substantiated in considering test problems, including the problem of steady and unsteady laminar flow of a viscous incompressible fluid along a circular cylinder.

With the aim of testing the developed methodology for a turbulent regime of flow along bodies we performed a complex numerical and experimental study of flow in a plane-parallel channel with a circular vortex cell on one of the walls. Undoubtedly, this investigation, apart from being methodological in nature, is also of substantative significance. Widely known are calculational and experimental works on analysis of circulating flow in rectangularly shaped trenches, in particular, in a square cavern [6-7]. However caverns of circular shape have been considered extremely rarely (see, for example, [8]) and most often in a simplified formulation, in particular, in motion of a moving boundary. In this work, not only a comparative analysis of calculational and experimental results seems interesting but also analysis of the effect of the thickness of the boundary layer that develops along the channel walls on the intensity of the vortex flow.

2. Flow in a channel with a transverse cylindrical hollow is investigated experimentally at the Institute of Mechanics of Moscow State University on a setup that is a small-sized direct-action wind tunnel in which the air flow is produced by a forced-draught fan. To equalize and damp the flow, in front of the nozzle we placed an elongated forechamber, in which a honeycomb and a grid for damping disturbances are installed. The forechamber is smoothly integrated with a planar profiled subsonic nozzle with a compression ratio of 4.0 that is connected to the setup's working channel manufactured of organic glass and having a rectangular cross sec-

Academy of Civil Aviation, St. Petersburg, Russia; Institute of Mechanics at M. V. Lomonosov Moscow State University, Russia. Translated from Inzhenerno-Fizicheskii Zhurnal, Vol. 73, No. 2, pp. 346-353, March–April, 2000. Original article submitted April 8, 1999.

1062-0125/00/7302-0337$25.00

tion of height $H = 0.05$ m and width $l = 0.08$ m. On the lower wall of the channel, plug-in units with different cylindrical hollows are installed. In operation, the cross section of the hollow was a circle with a diameter of 0.06 m, and the length of the inlet section $L = 0.052$ m was taken as the characteristic length. The horizontal walls of the channel can diverge smoothly by an angle of 10°, thus enabling us to produce flows with the required longitudinal pressure gradient. The fan and the nozzle provide a uniform flow with a head of 0.2–1.5 kPa at the inlet to the working channel, which corresponds to regimes with flow velocities U in the range of 15–50 m/sec (U is selected as the characteristic velocity).

Pressure was measured with tilted micromanometers. When the static pressure on the channel walls was determined, a 48-channel automatic pneumocommutator of the Central Aerohydrodynamics Institute was used for connecting drainage points. The total and static pressures in the flow and near the surfaces in different cross sections of the channel were measured with pneumoprobes moved by a traverse gear with a micrometer screw (the vernier reading is 0.05 mm).

The mutual arrangement of the channel cross sections in which the measurements were performed is determined by a Cartesian coordinate system where the lower wall of the channel is located in the plane $y = 0$, the lateral walls correspond to the planes $z = \pm z_0$ ($2z_0 = l/L = 1.54$), the x axis is directed streamwise, and the left edge of the hollow passes through the origin of coordinates.

The measurements of the static pressure in three cross sections of the channel ($x_1 = 1.06$, $x_2 = 0.5$, and $x_3 = 1.96$) permitted the conclusions:

a) of a weak effect of the channel's lateral walls that can be disregarded for cross sections $z < 0.8z_0$, as demonstrated by the practically constant pressure over the channel width measured using drainage holes on the lower wall of the channel and at the bottom of the cylindrical hollow;

b) of a practically constant static pressure along the channel height in the cross sections ahead of the hollow and behind it;

c) of the presence of intense vortex flow in the cylindrical hollow, as demonstrated by the behavior of the static pressure on its lateral wall (an example is given below in Fig. 3c).

The first of the indicated properties of the flow was decisive in selecting a two-parameter computational model.

The relative magnitude of longitudinal-velocity pulsations at the inlet to and the outlet from the working channel of the setup was measured by a DISA constant-resistance hot-wire anemometer (model A55).

Flow in the cylindrical hollow and its vicinity was visualized using the method of a hot wire (the method of smoke jets). A thin Nichrome filament 0.3–0.5 mm in diameter heated by an electric current was installed at the center of the cylindrical hollow in the vertical plane that was normal to the channel's longitudinal axis. Smoke was formed by combustion of an oil flowing down along the hot filament. The oil was fed through an upper current duct that was a copper tube 1 mm in diameter, in which the Nichrome filament ran. The intensity (optical density) of the smoke, dependent on the filament temperature, could be controlled smoothly. For observation of the flow pattern the required illumination (for example, a light plane) was created, and registration was performed using video tape recording.

Figure 1a presents a frame from a photogram of the flow obtained from a video tape for a velocity of the incoming flow $U = 36$ m/sec and a Reynolds number $\mathrm{Re} = 1.34 \cdot 10^5$, which is calculated from the distance L between the hollow's edges. The process of washing out of the smoke, which leads to almost uniform distribution of it in the cavity, indicates a turbulent regime of internal flow. We can clearly trace a separating surface formed when the external and internal flows meet near the leading edge of the hollow, which is visualized in the photographs as a boundary that separates the region filled with smoke from the external flow and runs between the edges. As the trailing edge is approached, this line becomes more washed out, which indicates an increased vorticity in the mixing layer.

On the whole, in the course of the experimental investigations we obtained data on the properties of gasdynamic flows near a planar wall with a cylindrical vortex cell for Reynolds numbers in the range of 10^4–$1.37 \cdot 10^5$ and for a turbulence level of 0.015 in the incoming flow. In spite of a pronounced turbulent character of the flow, in the averaged flow we can single out elements of a classical schematization of the sepa-

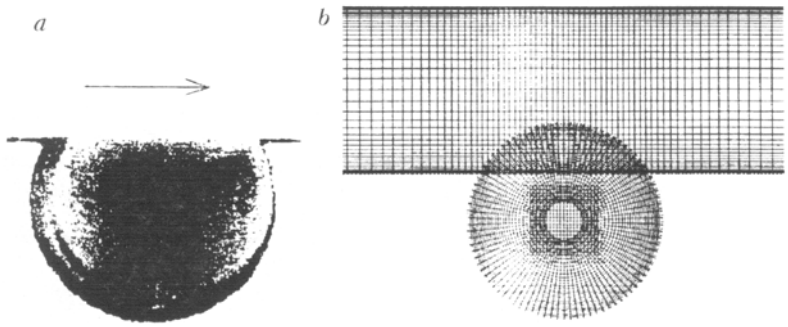

Fig. 1. Smoke visualization of the circulating flow in a circular cavern on the wall of a plane-parallel channel with a velocity of the incoming flow U = 36 m/sec and a Reynolds number Re = $1.34 \cdot 10^5$ (a) and a fragment of the multiblock computational grid (b).

rated-flow structure: shear and boundary layers and a core of return flow with constant vorticity. Inside the cylindrical cell, we observe, on the average, stable flow that is characterized by the presence of one large-scale vortex separated from the external flow by a shear mixing layer. The center of the vortex is shifted from the center of the circle and is localized to the vicinity of the "center of the area" of the cross section of the cell. The minimum pressure on the cell walls is attained at the point of maximum depth. The bend of the center streamlines and the transverse pressure gradient (in the region of the flow just above the cell) are small, while the profile of the average velocity in the exterior part of the shear layer is analogous to the Hertler classical turbulent profile for planar mixing layers. It should be noted that the experiments were carried out for two boundary-layer thicknesses of 0.04 and 0.1 in the incoming flow determined at a distance of 1.1 from the sharp edge upstream.

3. Numerical modeling of the flow of an incompressible viscous fluid in a channel with a circular cavern is considered within the framework of a two-dimensional approach based on finite-volume solution of Reynolds equations that are closed using two-parameter turbulence models. As the latter, one uses a high-Reynolds dissipative k–ε model that is popular in the practice of engineering calculations and Menter's low-Reynolds k–ε SST model, which showed good performance as applied to typical wall flows, including flows with flow separation. In the indicated model of Menter [9, 10], k–ω equations of the Saffman–Wilcocks low-Reynolds model are solved only inside the boundary layer, while the standard k–ε model is used in all the remaining zones of the flow. Menter transformed the standard k–ε model into a k–ω form and introduced a weight function F_1 that is equal to unity inside the region and decreases gradually to zero as the edge of the boundary layer is approached. The resultant equations for k and ω are represented in the form

$$\frac{D\rho k}{Dt} = \tau_{ij}\frac{\partial u_i}{\partial x_j} - \beta^*\rho\omega k + \frac{\partial}{\partial x_j}\left[\left(\mu + \sigma_k \mu_t \frac{\partial k}{\partial x_j}\right)\right],$$

$$\frac{D\rho\omega}{Dt} = \frac{\gamma}{\nu_t}\tau_{ij}\frac{\partial u_i}{\partial x_j} - \beta\rho\omega^2 + \frac{\partial}{\partial x_j}\left[\left(\mu + \sigma_\omega \mu_t \frac{\partial \omega}{\partial x_j}\right)\right] +$$

$$+ 2(1 - F_1)\rho\sigma_{\omega 2}\frac{1}{\omega}\frac{\partial k}{\partial x_j}\frac{\partial \omega}{\partial x_j}.$$

The constants φ of the new model are calculated from sets of the constants φ_1 and φ_2 in the following manner:

$$\varphi = F_1\varphi_1 + \varphi_2(1 - F_1).$$

For the first system of equations (according to Wilcocks): σ_{k1} = 0.85; $\sigma_{\omega 1}$ = 0.5; a_1 = 0.31; β_1 = 0.0750; β^* = 0.09; κ = 0.41;

$$\gamma_1 = \beta_1/\beta^* - \sigma_{\omega 1}\kappa^2/\sqrt{\beta^*}\,.$$

The constants of the second system of equations (the standard k–ε model) are: $\sigma_{k2} = 0.5$; $\sigma_{\omega 2} = 0.5$; $\beta_2 = 0.0750$; $\beta^* = 0.09$; $\kappa = 0.41$;

$$\gamma_2 = \beta_2/\beta^* - \sigma_{\omega 2}\kappa^2/\sqrt{\beta^*}\,.$$

Here

$$\tau_{ij} = \mu_t\left(\frac{\partial u_i}{\partial x_j} + \frac{\partial u_j}{\partial x_i} - \frac{2}{3}\frac{\partial u_k}{\partial x_k}\delta_{ij}\right) - \frac{2}{3}\rho k\delta_{ij}\,;\quad F_1 = \tanh\left(\arg_1^4\right);$$

$$\arg_1 = \min\left[\max\left(\frac{\sqrt{k}}{0.09\omega y}\,;\ \frac{500\nu}{y^2\omega}\right);\ \frac{4\rho\sigma_{\omega 2}k}{CD_{k\omega}y^2}\right],$$

where y is the distance to the surface; $CD_{k\omega}$ is the positive part of the cross diffusion terms in the equation of ω transfer,

$$CD_{k\omega} = \max\left\{2\rho\sigma_{\omega_2}\frac{1}{\omega}\frac{\partial k}{\partial x_j}\frac{\partial \omega}{\partial x_j},\ 10^{-20}\right\}.$$

The term $\arg_1$ obviously tends to zero with distance from the solid wall, since expressions of the type $1/y$ and $1/y^2$ are present in all its components. Inside the boundary layer, the first term is the ratio of the turbulence scale to the distance from the wall and is equal to 2.5 in the logarithmic layer and disappears as the boundary of the layer is approached. The second term points at F_1 being equal to unity within the sublayer (i.e., at F_1 precluding the use of a two-parameter dissipative turbulence model); here, ω behaves as $1/y^2$ near the wall and is proportional to $1/y$ in the logarithmic zone, so $1/(y^2\omega)$ is a constant in the vicinity of the wall and tends to zero in the logarithmic zone. The third argument assures $\arg_1$ tending to zero by blocking the dependence of the solution on the external-flow parameters. Since $\arg_1 \to 0$ on the edge of the boundary layer, F_1 becomes such that a standard high-Reynolds dissipative two-parameter model is employed in this zone.

We recommend employing the following parameters in the free flow:

$$\omega_\infty = (1 \to 10)\frac{U_\infty}{L_\infty}\,;\quad \nu_{t\infty} = 10^{-(2\to 5)}\nu_\infty\,;\quad k_\infty = \nu_{t\infty}\omega_\infty\,,$$

where L_∞ is the tentative length of the computational domain.

The boundary condition for ω on the solid wall ($y = 0$) is

$$\omega = 10\frac{6\nu}{\beta_1(\Delta y)^2}\,,$$

where Δy is the wall step. This condition is acceptable for smooth walls $\Delta y^+ < 3$.

The turbulent-viscosity factor is determined as

$$\nu_t = \frac{a_1 k}{\max(a_1\omega\,;\ \Omega F_2)}\,,$$

$$F_2 = \tanh\left(\arg_2^2\right),\quad \arg_2 = \max\left[2\sqrt{k}/(0.09\omega y)\,;\ \frac{500\nu}{y^2\omega}\right].$$

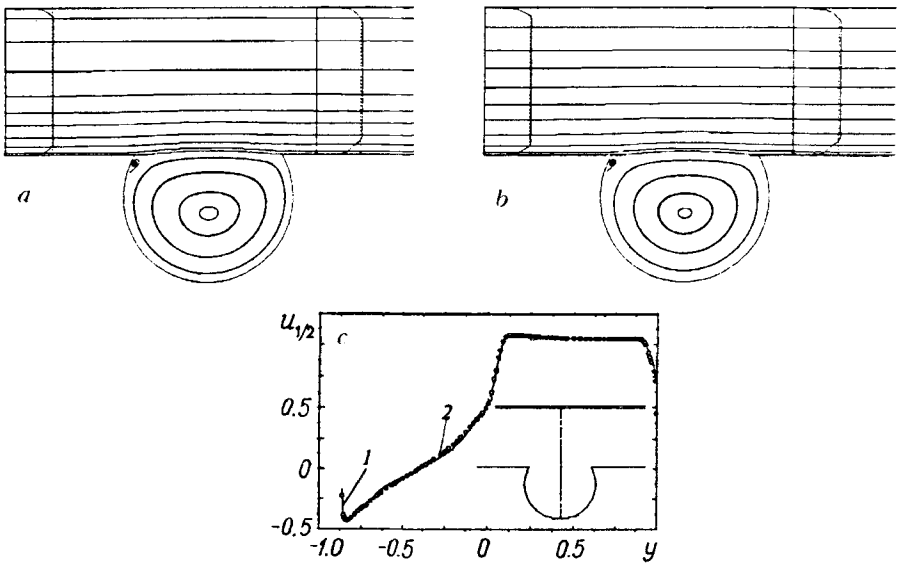

Fig. 2. Comparison of the flow patterns in a channel with a circular cavern obtained with a high-Reynolds two-parameter dissipative turbulence model (a) and Menter's low-Reynolds model (b) and the profiles of the longitudinal velocity component in the middle cross section of the cavern (c): 1) curve obtained based on the use of Menter's model; 2) data of calculations by the k–ε turbulence model.

The details of an implicit finite-volume computational procedure that is based on the concept of splitting by physical processes and a multiblock grid strategy are presented in [4, 11].

The steady turbulent flow of an incompressible viscous fluid in a plane-parallel channel of length 10 with a circular cavern, whose sharp edge is a distance of 4.5 from the inlet section, is calculated for a Reynolds number of $1.3 \cdot 10^5$. At the inlet to the channel, we prescribe a uniform velocity profile in the flow core and a "1/7" profile in the wall zones that develops in a boundary layer of prescribed thickness δ_{bl}. The inlet characteristics of turbulence correspond to the conditions of the physical experiment carried out. On the channel and cavern walls, we set an adhesion condition using Menter's low-Reynolds turbulence model or we use the apparatus of wall functions in the case of the high-Reynolds dissipative k–ε model [7]. At the outlet from the channel, we employ "mild" boundary conditions or the conditions of continuation of the solution. The boundary-layer thickness at the inlet to the channel is varied from 0 to 0.16 in the course of the numerical investigations.

The multiblock computational grid includes a rectangular grid in the channel proper that contains 81 $\times$ 61 nodes with bunching in the wall zones and in the vicinity of the sharp edges and a cylindrical grid in the circular cavern with a uniform distribution of the nodes in the circumferential direction (31 nodes on the arc outside the cavern) and a nonuniform distribution with bunching as the wall is approached (41 nodes in the radial direction). The wall steps are prescribed to be 10^{-3}. A "patch" – a 0.45 $\times$ 0.45 square grid that contains 21 $\times$ 21 nodes – is superimposed on the central zone of the cavern at the site of location of the axis of the cylindrical grid (Fig. 1b).

4. Figures 2-4 present some of the numerical and experimental results obtained.

To check the adequacy of the numerical predictions, we performed a comparative analysis of the results of calculating the flow in a channel with a circular cavern based on employment of the high-Reynolds version of the two-parameter dissipative model and Menter's low-Reynolds two-parameter model. It should be noted that in the first case the problem is solved on a coarser computational grid owing to the use of the apparatus of wall functions. Thus, the number of computational nodes is decreased to 41 in the cross section of the channel and to 31 in the radial direction of the cylindrical grid in the circular cavern, the wall step of

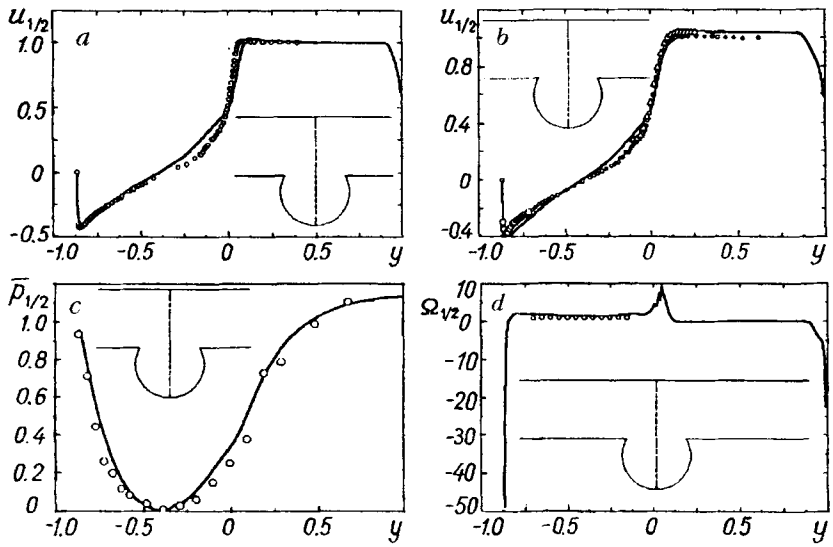

Fig. 3. Comparative analysis of calculational (curves) and experimental (points) results in the middle cross section of the cavern: profiles of the longitudinal velocity component for a boundary-layer thickness $\delta_{bl} = 0.04$ (a) and 0.10 (b) in the channel cross section $x = -1.06$, distributions of the reduced static pressure $\bar{p}$ (c) and the vorticity (d); c and d correspond to $\delta_{bl} = 0.1$.

the grid being increased to $5 \cdot 10^{-3}$ in the channel and to $9 \cdot 10^{-3}$ in the cavern. It should be noted that at the inlet to the channel we prescribed a profile with a very thin (of the order of 0.01) boundary layer in the variants considered.

Comparison of the results in Fig. 2 shows absence of an effect of the selected turbulence model on the solution, which indicates to a certain extent the correctness of the performed numerical modeling of the circulating flow in the cavern.

In the circular cavern, a very intense (with a velocity of about 0.45) circulating flow is realized whose structure is quite in agreement with the smoke-visualized pattern shown in Fig. 1a. The existence of the secondary vortices noted in the cavern in the numerical modeling (Fig. 2a and b) seemingly was quite attributable to the difference in the boundary-layer thickness at the inlet to the channel in the calculations (0.01) and the experiment (0.1). However the above vortex structure is also retained at $\delta_{bl} = 0.1$, and therefore the occurrence of the secondary vortices is associated rather with the two-dimensional character of the calculated flow. The center of the large-scale vortex is located in the middle cross section in the immediate vicinity of the center of gravity of the circular cavern ($y = -0.395$), which also correlates well with the experimental data ($y = -0.38$). We note that the geometric center of the cavern is somewhat above at a point with the coordinates ($x = 0.5$; $y = -0.29$). Another interesting feature is noteworthy: the streamline that separates the channel flow and the large-scale vortex flow of the fluid and practically connects the cavern's sharp edges has some convexity toward the external flow, which is quite in agreement with the pattern of the separated flow of an ideal fluid in a channel with a rectangular trench [12].

The conclusion of the adequacy of the numerical predictions performed based on the use of Menter's turbulent model can also be drawn from a comparative analysis of the calculated and experimental data in Fig. 3. For this purpose, we select a wide variety of local characteristics of the flow: the longitudinal velocity component, reduced static pressure, and vorticity taken in the middle cross section of the circular cavern. The reduced static pressure is determined as $\bar{p} = (p - p_m)/(p_c - p_m)$, where p is the static pressure at the center of the large-scale vortex and p_c is the pressure in the middle of the channel ($x = 0.5$; $y = 0.5$; $z = 0$).

We note the quite satisfactory agreement between the calculated and experimental data, especially as regards the profiles of the longitudinal velocity component in the middle cross section of the cavern. The dis-

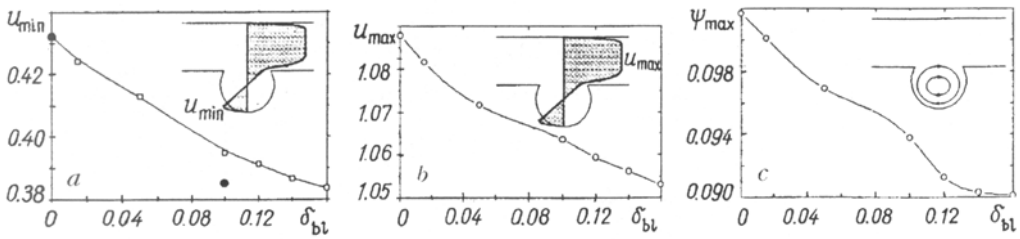

Fig. 4. Numerical analysis of the effect of the boundary-layer thickness at the inlet to the channel (x = 4.5) on the return-flow velocity that is maximum in absolute value (a) (the dark points are the experimental data), on the maximum of the longitudinal velocity component in the middle cross section of the cavern (b), and on the maximum of the current function (c).

agreement occurring, which refers to a great extent to the static-pressure distribution at the center of the cavern, should be assigned to the difference of the spatial character of the flow in the experimental analog from the character of the model two-dimensional flow.

We should note the good agreement between the calculated and experimental data on the vorticity in the core of the large-scale vortex flow in the cavern. It is of interest that the existence of a zone of practically constant vorticity in the cavern correlates well with the well-known model of J. Batchelor [5, 7], in accordance with which an ideal vortex of constant vorticity surrounded by a thin boundary layer is realized in the cavern when Re $\to \infty$. By and large the calculations confirmed the validity of the indicated concept, the more so that the evaluation of the characteristics of turbulence and, in particular, the vortex viscosity indicates their extremely low level in the vortex-flow core.

The last block of calculated data of Fig. 4 is concerned with the effect of the boundary-layer thickness in the incoming flow on extremum, local, and integral characteristics of the flow. Although the vortex pattern remains practically constant in the considered range of variation of δ_{bl}, the intensity of the return flow in the cavern becomes noticeably weaker as the boundary-layer thickness increases. The decrease observed in the maximum velocity of the channel flow can easily be explained by the decrease in the convexity of the separating streamline, which approaches a straight line connecting the sharp edges of the cavern.

The authors are grateful to Academician G. G. Chernyi for useful discussions of the problem.

The work was carried out with financial support from the Russian Fund for Fundamental Research, projects Nos. 99-01-01115 and 99-01-00722.

NOTATION

x_i, longitudinal, vertical, and transverse Cartesian coordinates (x, y, z) for i = 1, 2, 3, respectively; u_i, longitudinal, vertical, and transverse velocity components (u, v, w) for i = 1, 2, 3, respectively; ρ, density; μ and ν, dynamic and kinematic viscosity of the medium ($\nu = \mu/\rho$); p, static pressure; $\bar{p}$, reduced static pressure, $\bar{p} = (p - p_m)/(p_c - p_m)$; H, channel height; l, channel width; L, distance between the sharp edges in the plane of the lower channel wall; U, flow velocity at the inlet to the channel; t, time that is made dimensionless by means of U and L; ψ, current function; Re, Reynolds number determined from the air density and viscosity, U and L; δ_{bl}, boundary-layer thickness; Ω, absolute value of the vorticity; k, kinetic energy of turbulent pulsations; ε, dissipation rate of turbulent energy; ω, specific dissipation of turbulent kinetic energy; $CD_{k\omega}$, positive part of the cross diffusion terms in the equation of ω transfer; μ_t, turbulent dynamic viscosity; ν_t, turbulent kinematic viscosity ($\nu_t = \mu_t/\rho$); F_1 and F_2, auxiliary functions; τ_w, surface-friction tension; τ_{ij}, components of the friction tensor; Δy, wall step; Δy^+, dimensionless wall step ($\Delta y^+ = \sqrt{\tau_w/\rho}\,\Delta y/\nu$); δ_{ij}, Kronecker tensor; κ, von Kármán constant; β, β^*, γ, σ_k, and σ_ω, constants of the turbulence models; φ, generalized constant of the turbulence model; arg, argument in the auxiliary functions F; a_1, Bradshaw structural parameter. Subscripts: i, j = 1, 2, 3; ∞, flow parameters in the free flow; 1/2, flow parameters in the middle cross section of the cavern; max and min, maximum and minimum values.

REFERENCES

1. P. A. Baranov, S. A. Isaev, Yu. S. Prigorodov, and A. G. Sudakov, *Pis'ma Zh. Tekh. Fiz.*, **24**, Issue 8, 33-41 (1998).
2. P. A. Baranov, S. A. Isaev, Yu. S. Prigorodov, and A. G. Sudakov, *Pis'ma Zh. Tekh. Fiz.*, **24**, Issue 17, 16-23 (1998).
3. P. A. Baranov, S. A. Isaev, Yu. S. Prigorodov, and A. G. Sudakov, *Inzh.-Fiz. Zh.*, **72**, No. 3, 568-571 (1999).
4. P. A. Baranov, V. L. Zhdanov, and A. G. Sudakov, *Numerical Analysis of Unsteady Flow along a Cylinder with the Introduction of Induced Vorticity in the Near Wake*, Preprint No. 5 of the Academic Scientific Complex "A V. Luikov Heat and Mass Transfer Institute" [in Russian], Minsk (1988).
5. A. V. Bunyakin, S. I. Chernyshenko, and G. Yu. Stepanov, *J. Fluid Mech.*, **358**, 283-297 (1998).
6. V. Ya. Bogatyrev and Yu. I. Dubnishchev, *Prikl. Mekh. Tekh. Fiz.*, No. 2, 76-86 (1976).
7. I. A. Belov, S. A. Isaev, and V. A. Korobkov, *Problems and Methods of Calculating Separated Flows of an Incompressible Fluid* [in Russian], Leningrad (1989).
8. I. A. Belov, I. P. Ginzburg, and S. A. Isaev, *Vestnik LGU*, No. 13, 41-50 (1976).
9. F. Menter, *AIAA J.*, **32**, No. 8, 1598-1605 (1994).
10. A. Hellsten, *Some Improvements in Menter's k–ω SST Turbulence Model*, AIPP Paper, No. 98-2554 (1998).
11. S. A. Isaev, N. A. Kudryavtsev, and A. G. Sudakov, *Inzh.-Fiz. Zh.*, **71**, No. 4, 618-631 (1998).
12. M. A. Lavrent'ev and B. V. Shabat, *Problems of Hydrodynamics and Their Mathematical Models* [in Russian], Moscow (1973).